Editors' Suggestion

Unveiling the spin-singlet states of two electron-hole pair complexes using two-photon excitation in a GaAs/AlAs quantum dot

S. Germanis,[1,*] P. Atkinson,[1] A. Bach,[1] R. Hostein,[1] R. Braive,[2,3,4] M. Vabre,[1] F. Margaillan,[1] M. Bernard,[1] V. Voliotis,[1] and B. Eble[1,†]

[1]*Sorbonne Université, CNRS, Institut des Nanosciences de Paris, 75005 Paris, France*
[2]*Université Paris-Saclay, CNRS, Centre de Nanosciences et de Nanotechnologies, 91120, Palaiseau, France*
[3]*Université Paris Cité, CNRS, Centre de Nanosciences et de Nanotechnologies, F-91120 Palaiseau, France*
[4]*Institut Universitaire de France (IUF), Paris, France*

(Received 25 April 2022; accepted 9 June 2022; published 23 June 2022)

We use two-photon excitation to create biexcitonic complexes with two electron-hole pairs in different orbital levels of a GaAs/AlAs quantum dot. In addition to *p*-shell emission of the biexcitonic triplet states generated by two-photon excitation, we observe additional higher-energy resonances which are a signature of the radiative cascade of two-photon excited singlet states. The detection of these signals obtained in a high excitation regime is made possible by the use of a waveguiding structure in which the quantum dots are inserted, allowing an orthogonal excitation and detection geometry with an excellent laser rejection.

DOI: 10.1103/PhysRevB.105.235430

I. INTRODUCTION

Generating on-demand indistinguishable entangled photons is an essential step in quantum information applications [1]. In quantum dots (QDs) this has been realized by using the biexciton-exciton radiative cascade, to create pairs of polarization-entangled photons [2]. In resonant two-photon excitation (TPE) schemes the biexcitonic state can be coherently prepared and this process leads to the generation of high-fidelity indistinguishable entangled photon pairs [3,4].

Here, we show that the TPE process can be extended to resonantly probe an excited biexcitonic state where the two electron-hole pairs of the biexciton occupy different energy levels in the QD. In InAs/GaAs QDs such excited biexcitonic states have been used to implement a protocol for photonic cluster state generation [5], initialized by sequences of two optical pulses with different frequencies. In this case the first frequency was used to coherently initialize a dark exciton (where the electron and hole spins are parallel), and the second, different frequency pulse, was to generate the additional electron-hole pair in a higher-energy level [6]. In contrast, here we demonstrate that TPE can address an excited biexciton using a single-color optical field.

In the following, we present a study of the emission of two *e-h* pairs in a single GaAs/AlAs QD by measuring both the radiative recombination between excited valence and conduction orbital levels and between ground valence and conduction levels. These TPE experiments highlight in particular the signature of the nonradiative cascade of the excited spin-singlet state which is extremely difficult to detect otherwise.

*germanis@insp.jussieu.fr
†benoit.eble@insp.jussieu.fr

II. SAMPLE DESCRIPTION AND OPTICAL CHARACTERIZATION

GaAs/AlAs QDs embedded in AlGaAs waveguides were grown by MBE. The experimental implementation of a two-photon excitation (TPE) experiment requires higher pump power than for one-photon processes. A good rejection of the laser is therefore necessary in order to accurately measure the luminescence of the dot. For that purpose, the dots were located in the middle of a 400-nm-thick $Al_{0.33}Ga_{0.67}As$ surrounded by 1-μm-thick $Al_{0.70}Ga_{0.30}As$ upper and lower cladding layers. To define the dots, 12–14 nm deep nanoholes were etched by Al droplet deposition on the $Al_{0.33}Ga_{0.67}As$ surface [7]. These nanoholes were overgrown by a thin 2-nm AlAs barrier, 1-nm GaAs layer, and a 2-nm AlAs top barrier. Net migration towards the nanohole during a brief, 15-s, growth interruption after the deposition of the 1-nm GaAs layer resulted in the formation of inverted GaAs dots with a height ∼4–6 nm.

One-dimensional (1D) waveguides were etched by inductively coupled plasma (ICP) on the surface of the sample yielding micrometer size ridges. The resulting 1D-guided mode is excited by a single-mode optical fiber positioned at the entrance of the ridge. The optical mode losses are low enough that the scattered laser light does not affect the QD signal which is collected perpendicularly by a microscope objective [see Fig. 1(a)].

Figure 1(b) shows a typical photoluminescence (PL) spectrum where the dot is excited by 6-ps pulses of a Ti-Sa laser at 80 MHz with excitation power above 100 μW. The laser energy is tuned ∼10 meV above the neutral exciton transition energy. As clearly seen in Fig. 1(b) highlighted by a blue shaded area, this strong excitation power gives rise to a signal ∼10 meV higher in energy than the laser energy. The 20-meV separation between the neutral exciton and this higher-energy peak corresponds to the typical p_h-p_e transition energy [8].

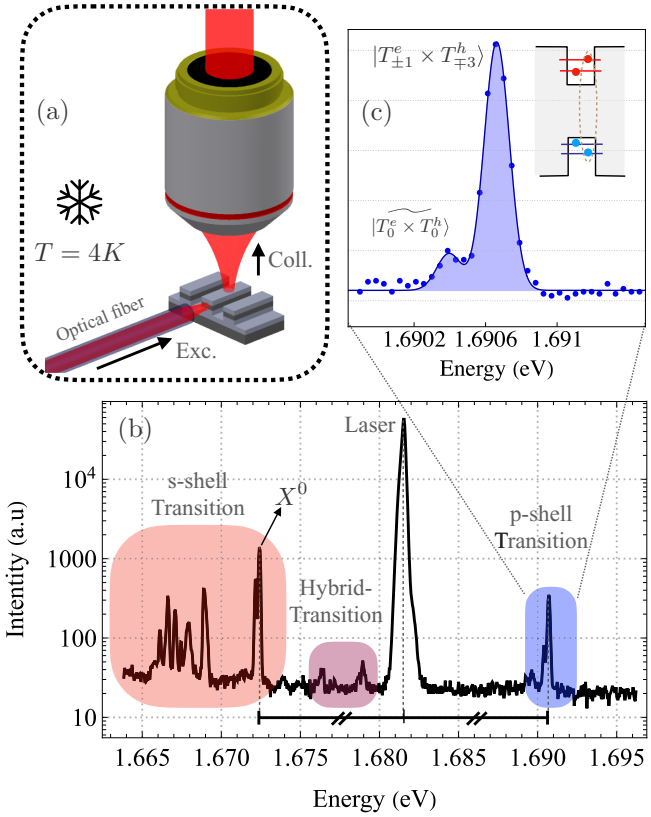

FIG. 1. (a) Sketch of the excitation and detection paths. An optical fiber focuses the laser beam onto the cleaved edge of the one-dimensional waveguide in which the dots are embedded. The luminescence is collected by a microscope objective along the growth direction. The optical fiber passes through an additional window of a MyCryoFirm optidry 250 ultralow vibration cryostat. (b) Log-scale broad PL spectrum of a quantum dot with the laser energy tuned exactly at the TPE resonance condition between the neutral exciton and the biexcitonlike complex $s^1_e s^1_h p^1_e p^1_h$. The colored shaded areas indicate the luminescence of optical transitions involving p_e-p_h (light blue), s_e-s_h orbital levels (light red), and s_e-p_h or p_e-s_h hybrid transitions (light purple). (c) Zoom on the p-shell emission region (linear scale) showing the doublet structure. The less intense low-energy peak denotes the recombination of $|T^e_0 \times T^h_0\rangle$ leaving a neutral exciton in the dot whereas the higher-energy peak corresponds to $T^e_{\pm1} \times T^h_{\mp3}$ (see text).

The intensity of this higher-energy line becomes almost comparable to that of the neutral exciton (X^0) when the excitation power exceeds ~100 μW. All the measured QDs (more than 10 on this sample and on another similar one) show the same characteristic spectral feature of a higher-energy line ~20 meV above the neutral exciton when the laser energy is ~10 meV above the neutral exciton. In the particular case of the results shown here, the high-energy line has a doublet structure [see Fig. 1(c)]. The number of high-energy lines varies from dot to dot and seems to be related to the relative PL intensity between the negative trion X^- compared to that of the neutral exciton X^0.

In the high excitation power regime a large number of emission lines can be seen at lower energy to X^0. These lines are related to the s-shell transitions [highlighted by a red frame on Fig. 1(b)]. These lines have been assigned to the neutral exciton X^0, the dark exciton [9–11], the negative trion X^-, and the biexciton XX^0 (see Supplemental Material [12]). Other peaks are likely to be other charged states. In addition, weak peaks [highlighted by a purple frame on Fig. 1(b)] are detected a few meV below the laser energy position. These weak features, at least two orders of magnitude less intense than X^0, appear also for other dots studied under the same excitation conditions. Their emission energies correspond to optical transitions involving recombination between electron and hole in different energy levels. The emission is weak due to poor wave-function overlap due to different spatial symmetry. These transitions will be referred to here as "hybrid" transitions and are discussed in more detail in Appendix C.

In the following, the origin of each group of PL lines will be discussed. However, the main text is limited to a comprehensive study of the p_h-p_e transitions, is presented providing a description of the mechanisms that lead to the higher-energy emissions, whereas Appendix C provides a confirmation focusing on hybrid transitions. The detection of optical p_h-p_e transitions is enhanced in these type of GaAs dots especially since the intersublevel relaxation time of the electron has been estimated to be several tens of picoseconds [13]. This relaxation time is more than an order of magnitude longer that observed in InAs dots [14].

III. TWO-PHOTON EXCITATION REGIME AND p_H-p_E TRANSITIONS

Figure 2(a) shows the high-energy doublet related to p-shell emission of the excited biexciton. To study this emission in more detail, Fig. 2(a) shows a PL intensity map of this doublet as a function of the PL energy and the energy of the pulsed laser scanned in a range of a few meV, around the maximum of PL intensity. The oblique white dashed line having the equation $E^{\text{doublet}}_{\text{PL}} = 2E_{\text{laser}} - E_{X^0}$ which traces the energy dependence of the doublet formally confirms the TPE process. The luminescence energy of the doublet located at ~20 meV above the exciton lines is consistent with recombination from the p levels [8]. We can therefore assign the doublet to the fine structure (FS) associated with a "biexciton" of type $s^1_e s^1_h p^1_e p^1_h$. In other words, this TPE process creates simultaneously an electron-hole (e-h) pair on the s-shell levels, and another one on the p levels, which is an unconventional excitation process. In the following discussion, only one conduction and valence p-envelope state will be considered since no experimental evidence allows to discriminate the role of the two distinct p levels.

To fully understand the observed spectroscopic signatures, we have to take into account the FS of the probed states. In particular, the FS of $s^1_e s^1_h p^1_e p^1_h$ is formed by $2^4 = 16$ states, nine of which are built on the basis of the triplets $\{|T^e_{-1,0,+1} \times T^h_{-3,0,+3}\rangle\}$, where $|T^h_{+3}\rangle = |\Uparrow_{s_h}\Uparrow_{p_h}\rangle$, $|T^h_{-3}\rangle = |\Downarrow^{s_h}\Downarrow^{p_h}\rangle$, and $|T^h_0\rangle = |\Uparrow_{s_h}\Downarrow^{p_h} + \Downarrow^{s_h}\Uparrow_{p_h}\rangle/\sqrt{2}$. Similar notation is used for the electronic triplets. The other seven states are built with higher-energy singlet states, such as $|S^{*,h}_0\rangle = |\Uparrow_{s_h}\Downarrow^{p_h} - \Downarrow^{s_h}\Uparrow_{p_h}\rangle/\sqrt{2}$ for the holes. Note that we use the notation $|S^h_0\rangle$ to refer to the holes singlet configuration involving only

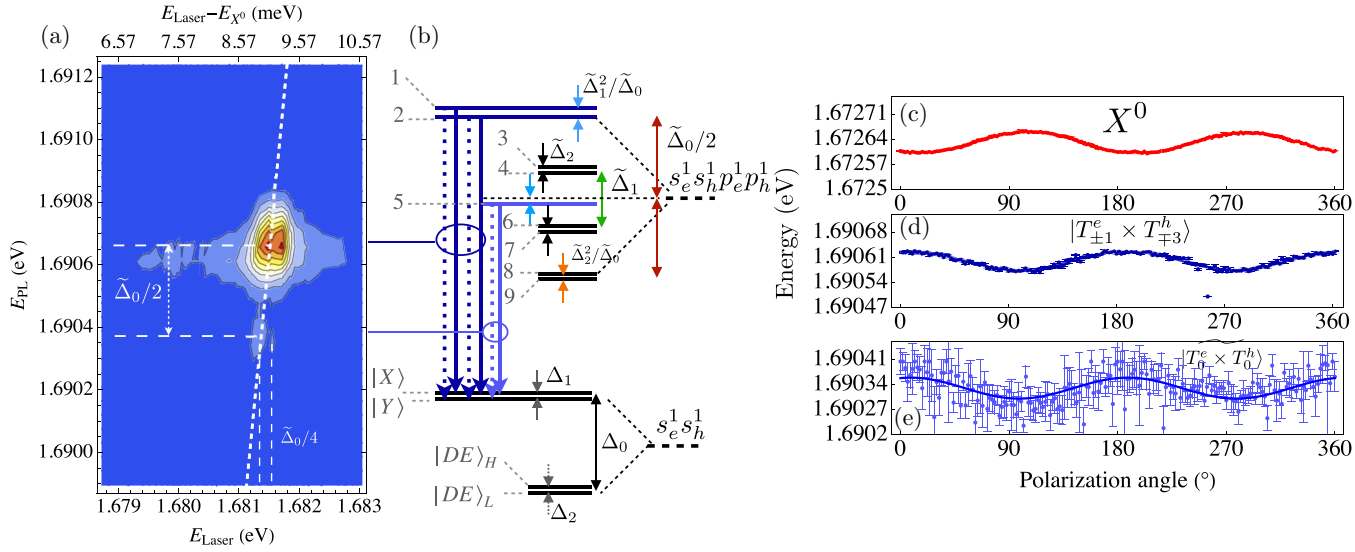

FIG. 2. (a) PL map of the doublet associated with the $s_e^1 s_h^1 p_e^1 p_h^1$ biexciton as a function of the pulsed laser energy. (b) Fine structure of $s_e^1 s_h^1 p_e^1 p_h^1$ limited to the subspace of triplet states. Head to tail arrows of the same color indicate identical splitting. The conventions $\widetilde{\Delta}_0 > 0$, $\widetilde{\Delta}_1 > 0$, and $\widetilde{\Delta}_2 > 0$ were used. To simplify the notation, Δ_0, Δ_1, Δ_2 have been written instead of $\Delta_0^{s_e s_h}$, $\Delta_1^{s_e s_h}$, $\Delta_2^{s_e s_h}$. $|X\rangle$ and $|Y\rangle$ denote the linear components of the bright exciton, and $|DE\rangle_H$, $|DE\rangle_L$ the high- and low-energy components of the dark exciton. The solid and dotted vertical lines map the linearly polarized *p*-shell biexcitons recombination towards the X and Y exciton components. Polarization-resolved PL energies for the neutral exciton (c), for $|T_{\pm1}^e \times T_{\mp3}^h\rangle$ (d), and $|\widetilde{T_0^e \times T_0^h}\rangle$ transitions (e). Note that the same vertical scale is used for (c), (d), and (e).

the s_h orbital, for example, present in the neutral biexciton state $XX^0 = s_e^2 s_h^2$.

The FS in the subspace of triplet states has already been derived in Ref. [15], in the single-particle approximation (SPA). This approximation holds in strongly confining dots such as InAs QDs and perfectly describes the FS associated with negatively charged excitonic complexes [16]. QDs characterized by a weaker confinement potential, such as GaAs dots, often require to go beyond this approximation by considering Coulombic correlations mixing all orbital levels as soon as an *e*-*h* pair is created in the dot [17–19]. A direct consequence of such many-body effects can lead to a deviation of the FS energy diagram from that estimated in the SPA [20].

In our case, we will show that the presence of the doublet observed in the PL spectrum under TPE condition comes from only three among the nine states forming the triplet subspace. Since the FS is far from being fully resolved, we will describe the energy diagram of $s_e^1 s_h^1 p_e^1 p_h^1$ in the framework of the SPA.

The Hamiltonian leading to the FS of $s_e^1 s_h^1 p_e^1 p_h^1$ reads as

$$\hat{H}_{eehh} = \sum_{\substack{i\in\{s_e,p_e\}\\ j\in\{s_h,p_h\}}} -\frac{2}{3}\Delta_0^{ij}\hat{S}_z^i\hat{J}_z^j + \frac{\Delta_1^{ij}}{2}(\hat{S}_+^i\hat{J}_-^j + \hat{S}_-^i\hat{J}_+^j) + \frac{\Delta_2^{ij}}{2}(\hat{S}_+^i\hat{J}_+^j + \hat{S}_-^i\hat{J}_-^j), \quad (1)$$

where $\hat{J}_{z,+,-}$ are the spin operators acting on the hole pseudospin one-half; $\hat{S}_{z,+,-}$ act on the electron spin. Δ_0^{ij} is the *e*-*h* isotropic exchange interaction between the electron i and the hole j, whereas Δ_1^{ij} is the anisotropic *e*-*h* exchange interaction contribution acting on the *e*-*h* pair (i, j) when it is bright, and Δ_2^{ij} when it is dark, i.e., made of parallel *e*-*h* spins.

The resulting FS is shown in Fig. 2(b) where the nine triplet states are labeled from $|1\rangle$ to $|9\rangle$ by order of decreasing energy. The splittings are simply expressed with a set of three parameters $\widetilde{\Delta}_0 = \sum_{i,j}\Delta_0^{ij}/2$ and $\widetilde{\Delta}_{1/2} = \sum_{i,j}\Delta_{1/2}^{ij}/8$. The eigenvectors, given in Table I, are expressed in the triplet-state basis, and are calculated in the limit where $\widetilde{\Delta}_0 \gg \widetilde{\Delta}_1 \gg \widetilde{\Delta}_2$.

The issue is now to determine to which of the nine triplet states correspond to the optical signatures observed in Fig. 2(a), considering both the *p*- and *s*-shell recombination. States $|8\rangle$ and $|9\rangle$ in Table I are built from states with dark spin configurations ($|T_{\pm1}^e \times T_{\pm3}^h\rangle$), and can therefore be discarded. Moreover, the recombination of a bright *e*-*h* pair from $|T_{\pm1}^e \times$

TABLE I. Decomposition of the states $1,\ldots,9$ shown in Fig. 2(b) as a function of the triplet states. The normalization is given at the lowest order in $\widetilde{\Delta}_1/\widetilde{\Delta}_0$. The states involved in the TPE experiments are in bold. Note that $|1\rangle$ denoted in the main text by $|\widetilde{T_0^e \times T_0^h}\rangle$ is a combination of $|T_0^e \times T_0^h\rangle$ and $|T_{-1}^e \times T_{+3}^h\rangle + |T_{+1}^e \times T_{-3}^h\rangle$ states.

No.	
$\|\mathbf{1}\rangle$	$(\|T_{-1}^e \times T_{+3}^h\rangle + \|T_{+1}^e \times T_{-3}^h\rangle)/\sqrt{2} + \frac{2\widetilde{\Delta}_1}{\sqrt{2}\widetilde{\Delta}_0}\|T_0^e \times T_0^h\rangle$
$\|\mathbf{2}\rangle$	$(\|T_{-1}^e \times T_{+3}^h\rangle - \|T_{+1}^e \times T_{-3}^h\rangle)/\sqrt{2}$
$\|3\rangle$	$(\|T_{+1}^e \times T_0^h\rangle + \|T_{-1}^e \times T_0^h\rangle + \|T_0^e \times T_{+3}^h\rangle + \|T_0^e \times T_{-3}^h\rangle)/2$
$\|4\rangle$	$(\|T_{+1}^e \times T_0^h\rangle - \|T_{-1}^e \times T_0^h\rangle - \|T_0^e \times T_{+3}^h\rangle + \|T_0^e \times T_{-3}^h\rangle)/2$
$\|\mathbf{5}\rangle$	$\|T_0^e \times T_0^h\rangle - \frac{\widetilde{\Delta}_1}{\widetilde{\Delta}_0}(\|T_{-1}^e \times T_{+3}^h\rangle + \|T_{+1}^e \times T_{-3}^h\rangle)$
$\|6\rangle$	$(\|T_{+1}^e \times T_0^h\rangle - \|T_{-1}^e \times T_0^h\rangle + \|T_0^e \times T_{+3}^h\rangle - \|T_0^e \times T_{-3}^h\rangle)/2$
$\|7\rangle$	$(\|T_{+1}^e \times T_0^h\rangle + \|T_{-1}^e \times T_0^h\rangle - \|T_0^e \times T_{+3}^h\rangle - \|T_0^e \times T_{-3}^h\rangle)/2$
$\|8\rangle$	$(\|T_{+1}^e \times T_{+3}^h\rangle - \|T_{-1}^e \times T_{-3}^h\rangle)/\sqrt{2}$
$\|9\rangle$	$(\|T_{+1}^e \times T_{+3}^h\rangle + \|T_{-1}^e \times T_{-3}^h\rangle)/\sqrt{2}$

$T_0^h\rangle$, $|T_0^e \times T_{\pm 3}^h\rangle$ leaves the dot with a dark *e*-*h* pair, indicating that these states would be addressed through a dark-exciton virtual state in the TPE process. As discussed in Appendix B, TPE is more probable if the virtual state has a large oscillator strength. However, we have already shown in Ref. [10] that in these dots the typical ratio of oscillator strengths between dark and bright pairs is ∼1:1000, even though the dark exciton luminescence signal can become comparable to the bright one under certain excitation conditions. We can exclude states where the TPE process would occur via a dark exciton virtual state, i.e., states $|3\rangle$, $|4\rangle$, $|6\rangle$, and $|7\rangle$. This leaves states $|1\rangle$, $|2\rangle$, and $|5\rangle$ as those addressed by the proposed TPE process. These states leaves a bright *e*-*h* in the dot after *p*-shell emission and are therefore accessed by a bright exciton virtual state in the TPE process.

The energy splitting between $|1\rangle$ and $|2\rangle$, $\widetilde{\Delta}_1^2/\widetilde{\Delta}_0$, can be estimated from the data shown in Fig. 2. The splitting energy $\widetilde{\Delta}_0/2 \sim 280\ \mu$eV can be quantified from the observed doublet energy splitting[1] shown in Fig. 2(a) and, on the other hand, $\widetilde{\Delta}_1$ can be approximated by $\Delta_1^{s_e s_h}/2$, with $\Delta_1^{s_e s_h} = 58\ \mu$eV being the bright exciton FS splitting deduced from polarization-resolved PL measurements of the neutral exciton [see Fig. 2(c)]. This leads $\widetilde{\Delta}_1^2/\widetilde{\Delta}_0$ to be estimated to ∼2 μeV. As a consequence, $|1\rangle$ and $|2\rangle$ are almost degenerate and will be labeled in the following $|T_{\pm 1}^e \times T_{\mp 3}^h\rangle$ with an energy $E_{|T_{\pm 1}^e \times T_{\mp 3}^h\rangle}$, while $|\widetilde{T_0^e \times T_0^h}\rangle$ with energy $E_{|T_0^e \times T_0^h\rangle}$ will refer to $|5\rangle$. The degeneracy of states $|1\rangle$ and $|2\rangle$ explains the appearance of a doublet structure on the *p*-shell emission side, although three triplet components are involved.

In further discussion, the laser energy for which the TPE condition is fulfilled for $|T_0^e \times T_0^h\rangle$ is labeled $E^L_{|T_0^e \times T_0^h\rangle}$, while the absolute energy for state $|T_0^e \times T_0^h\rangle$ is labeled as $E_{|T_0^e \times T_0^h\rangle}$.

The interpretation given above is consistent with the results in Figs. 2(d) and 2(e) which show the *p*-shell recombination energy of $|T_{\pm 1}^e \times T_{\mp 3}^h\rangle$ and $|\widetilde{T_0^e \times T_0^h}\rangle$ as a function of the polarization angle. The same FS splitting amplitude as the neutral exciton (Fig. 2) but with a π-phase shift is observed with respect to the neutral exciton [Fig. 2(a)] confirms that X^0 is the final state of both *p*-shell optical transitions. In order to confirm the arguments developed above, we present in the Supplemental Material [12] the spectroscopy of the triplet biexcitonic states from the point of view of *s*-shell recombinations, using TPE resonances excited with a cw laser.

For higher pump powers (∼200 μW), when the laser is scanned above the TPE condition, new absorption resonance is observed. These resonances originating of the *p*-shell recombination $|\widetilde{T_0^e \times T_0^h}\rangle$ appear spectrally broader than those studied so far, and are labeled α_1, α_2, α_3, and α_4 in Fig. 3(a).

Similar resonances are found for $|T_{\pm 1}^e \times T_{\mp 3}^h\rangle$ [Fig. 3(b)] and no energy shift is observed with respect to the $|\widetilde{T_0^e \times T_0^h}\rangle$ resonances. However, the shift of $\widetilde{\Delta}_0/4 = E^L_{|T_{\pm 1}^e \times T_{\mp 3}^h\rangle} - E^L_{|T_0^e \times T_0^h\rangle}$ is observed between the two, previously assigned, triplet TPE resonances as expected and displayed on Fig. 3(b).

[1] $\widetilde{\Delta}_0/2$ has to be compared with $\Delta_0^{s_e s_h} \sim 240\ \mu$eV, and are of the same magnitude.

We have also observed these resonances using continuous wave (cw) laser excitation, and detecting the neutral biexciton in the *s* shell, i.e., after the additional relaxation of the hot triplet to the biexciton (see Supplemental Material [12]).

The additional lines lie on a continuumlike background fitted by a quadratic dependance [21] with the laser energy [dashed lines in Figs. 3(a) and 3(b)]. This background signal remains measurable well below the TPE energy $E^L_{|T_0^e \times T_0^h\rangle}$. This indicates the existence of a dot filling mechanism, in the high excitation power regime, such as Auger processes in the GaAs matrix, and/or by a charge transport via the *X*-valley states confined in the high concentration aluminum barriers [22].

We will show that these resonances correspond to emission from the triplet states after TPE of the higher-energy states labeled $|\alpha_i\rangle$. They involve in particular the singlet components $(s_e^1 s_h^1 p_e^1 p_h^1)_{\text{singlet}}$ for at least the first two resonances, i.e., α_1 and α_2 [see Fig. 3(b)].

The energy separation of these additional states from the X^0 energy $E_{|X^0\rangle}$ can be easily estimated according to

$$E_{|\alpha_n\rangle} - E_{|X^0\rangle} = 2E^L_{|\alpha_n\rangle} - E_{|X^0\rangle}, \tag{2}$$

where $E^L_{|\alpha_n\rangle}$ is the laser energy tuned to the TPE condition of the state $|\alpha_n\rangle$ having an energy $E_{|\alpha_n\rangle}$.

Provided that the $|\alpha_n\rangle$ are two excited biexciton states, they should partially relax nonradiatively on the spin-singlet biexciton XX^0. As a consequence, the energy $E_{|\alpha_n\rangle} - E_{|X^0\rangle}$ corresponds to an absorption resonance that should be found in the excitation of the luminescence (PLE) spectrum of XX^0. Note that the energy $E_{|\alpha_n\rangle} - E_{|X^0\rangle}$ takes into account the Coulomb renormalization in the definition of $E_{|\alpha_n\rangle}$. These resonances are all present in the PLE spectrum of XX^0 in Fig. 3(c).

This indicates that $|\alpha_n\rangle$ can decay via the nonradiative and radiative cascade $\alpha_n \to XX^0 \rightsquigarrow X^0$, as well as via the cascade $\alpha_n \to (s_e^1 s_h^1 p_e^1 p_h^1)_{\text{triplet}} \rightsquigarrow X^0$ which gives rise to the resonances seen in Figs. 3(a) and 3(b). Due to the biexciton-exciton radiative cascade, the same resonances are also found in the X^0 PLE spectra (see the Supplemental Material [12]). The corresponding $\{\alpha_n\}$ resonances are marked on the PLE spectra by colored rectangles centered on the position of the resonance according to Eq. (2) and with width corresponding to the width at half-maximum of the resonances of Fig. 3(a) evaluated by a Gaussian deconvolution.

It is then remarkable to note that the experiments of Figs. 3(a) and 3(b) on the one hand, and of Fig. 3(c) on the other hand, optically probe the same excitations with different laser energies. This is related to the difference in excitation conditions. Under high-power pulsed excitation (200 μW), the state $|\alpha_n\rangle$ is directly generated by two-photon absorption via a virtual state. However, under the continuous excitation conditions used for the PLE measurements, once the QD traps an *e*-*h* pair, the coherent photocreation of a second *e*-*h* pair will leave the dot in the state $|\alpha_n\rangle$ as shown in the insert to Fig. 3(c).

PLE was performed by using a cw laser with a step tuning of 120 μeV. Note that the laser energy range used in the PLE does not exceed the GaAs one LO-phonon energy (36 meV) with respect to the X^0 emission. According to Ref. [23], we can thus safely exclude phononic resonances in the XX^0 PLE.

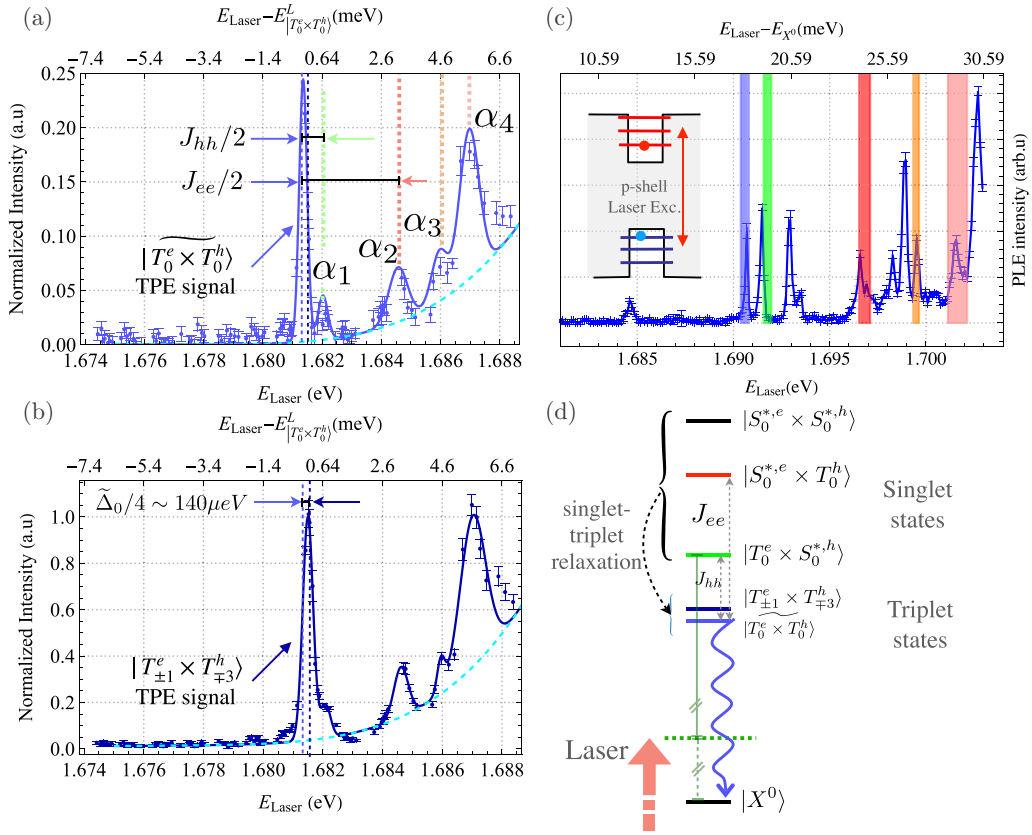

FIG. 3. (a) Evolution of the *p*-shell emission of $|\widetilde{T_0^e\times T_0^h}\rangle$ where the *ps*-laser energy is scanned through the TPE resonance. The laser power is set close to the maximum, ∼200 μW. The dashed line is the estimated background whereas the solid line is a guide to the eyes deduced from a Gaussian deconvolution. α_1, α_2, α_3, and α_4 label the high-energy resonances, indicated by vertical colored lines. (b) Same graph for $|T^e_{\pm1}\times T^h_{\mp3}\rangle$. (c) cw-PLE spectrum of the biexciton XX^0. The resonance associated with the states $|\alpha_n\rangle$ is highlighted with rectangles with the same color code as in (a). The inset illustrates the presence of resonances and the role of $\{\alpha_n\}$ states, by a sequential absorption process, where an *e*-*h* pair is already present in the dot. (d) Energy-level diagram showing the TPE of the singlet components, the possible relaxation mechanisms down to the triplet followed by the triplet emission. For clarity, only the $|T_0^e\times S_0^{*,h}\rangle$ excitation has been illustrated. The corresponding TPE condition is indicated by the horizontal green dashed line placed at the laser energy for the α_1 resonance in (a), while the absolute energy of $|T_0^e\times S_0^{*,h}\rangle$ is indicated by the position of the green rectangle in (c).

The first identified resonance at 1.6905 eV is the one associated with the cascade of a triplet state to the biexciton. The width of this resonance is about 345 μeV and does not allow to discriminate between $|\widetilde{T_0^e\times T_0^h}\rangle$ and $|T^e_{\pm1}\times T^h_{\mp3}\rangle$ which are split by 280 μeV.

The next resonances corresponding to α_1 and α_2 are, respectively, located at 1.3 and 6.2 meV in Fig. 3(c). Similar energy separations have also been measured by magneto-optics experiments in GaAs/AlGaAs QD [24]. These values are consistent in magnitude with the magnitude of the *h*-*h* exchange interaction J_{hh} and the *e*-*e* exchange interaction J_{ee}, which governs the splitting between the hole triplet T_0^h and the excited singlet $S_0^{*,h}$, and between the triplet T_0^e and excited singlet $S_0^{*,e}$, respectively.

The schematic diagram of Fig. 3(d) then explains the resonances observed in Figs. 3(a) and 3(b), and illustrates in particular the TPE process leading to the resonance α_1, which is related to the state $|T_0^e\times S_0^{*,h}\rangle$. The addressing of the singlet states $|T_0^e\times S_0^{*,h}\rangle$ for α_1 and $|S_0^{*,e}\times T_0^h\rangle$ for α_2 by TPE, followed by a nonradiative relaxation, populates the triplet $|\widetilde{T_0^e\times T_0^h}\rangle$ or $|T^e_{\pm1}\times T^h_{\mp3}\rangle$ states, increasing their respective signal intensities. Although the $|T^e_{-1,0,+1}\times S_0^{*,h}\rangle$ (respectively $|S_0^{*,e}\times T^h_{-3,0,3}\rangle$) states are degenerate due to their spin-singlet nature, we attribute the two-photon resonance at α_1 only to $|T_0^e\times S_0^{*,h}\rangle$ (and that of α_2 to $|S_0^{*,e}\times T_0^h\rangle$) since for the $|T^e_{\pm1}\times T_0^h\rangle$ and $|T_0^e\times T^h_{\pm3}\rangle$ states, the virtual state would be dark excitons (see Appendix B). As a consequence, only $|T_0^e\times S_0^{*,h}\rangle$ and $|S_0^{*,e}\times T_0^h\rangle$ are addressable by TPE. A confirmation of the $|T_0^e\times S_0^{*,h}\rangle$ TPE is given in Appendix C. There we show that since $|T_0^e\times S_0^{*,h}\rangle$ can efficiently relax to $|T_0^e\times S_0^h\rangle$, its TPE resonance can be also monitored by the hybrid transitions [see Fig. 6(e)].

The presence of the higher-energy resonances shown in Figs. 3(a) and 3(b) indicates an efficient nonradiative relaxation process from the excited spin-singlet states to the spin-triplet states. Since the energy difference between the states is only a few meV, this relaxation is assisted by acoustic phonon emission. The hot singlet states $|S_0^{*,e/*,h}\rangle$ are not easily detected in emission since they can efficiently thermalize to $S_0^{e/h}$ without spin flip, giving rise to a signal in the XX^0 PLE [Fig. 3(c)]. Nevertheless, this relaxation competes with another channel assisted by *e*-*h* flip-flop, leading to the triplet

states occupancy with an efficiency rate [25,26]

$$\gamma_{f,i} \sim \left(\frac{M_{f\leftarrow i}}{D_{f,i}}\right)^2 \tau_{ph}^{-1}(D_{f,i}), \tag{3}$$

where f denotes one of the triplet states, i one of the singlet states, $D_{f,i}$ is the energy difference, and $\tau_{ph}^{-1}(D_{f,i})$ is the emission rate of acoustic phonons with an energy $D_{f,i}$. $M_{f\leftarrow i}$ is the coupling between f and i, which can be driven in first consideration by the e-h exchange interaction $\hat{H}_{eehh}$.

Table II of Appendix A shows the matrix elements between the three hot singlet states, and the three final triplet states: the two almost degenerate states $|1\rangle$ and $|2\rangle$ and the lower-energy state $|5\rangle = |T_0^e \times T_0^h\rangle$. In particular, we note that the matrix element for the two lowest-energy spin-singlet states with the state $|T_0^e \times T_0^h\rangle$, i.e., $|5\rangle$ is zero, and so a relaxation process driven by the e-h anisotropic exchange interaction cannot be used to explain the α_1 and α_2 resonances seen in Fig. 3(a). The same is true for states $|1\rangle$ and $|2\rangle$ which have a symmetric and an antisymmetric combination of $|T_{\pm1}^e \times T_{\mp3}^h\rangle$, and a zero matrix element with the lowest-energy hot-singlet states. Instead, nonradiative decay path from the hot singlet to the p-shell triplet states is made possible by the spin-orbit-induced anisotropic part of the e-e exchange interaction which mixes $S_0^{*,e}$ and T_0^e [25,27,28]. This interaction, which causes the inversion of the circular polarization of the hot trion luminescence, has already been identified in the same GaAs dot [8]. It is worth mentioning that the anisotropic part of the e-e exchange interaction mixing $|T_0^e\rangle$ and $|S_0^{*,e}\rangle$ also assists a relaxation from $|T_0^e\rangle$ to $|S_0^e\rangle$. This additional relaxation mechanism is highlighted in Appendix C where the selective two-photon excitation of $|T_0^e \times T_0^h\rangle$ enhances the $|S_0^e \times T_0^h\rangle$ signal measured through hybrid transitions [see Fig. 6(e)]. Moreover, the anisotropic spin-orbit interaction can also act on valence states by coupling $|T_0^h\rangle$ and $|S_0^{*,h}\rangle$ [20,29] opening additional relaxation channels between singlet and triplet.

Now that the origin of α_1 and α_2 resonances have been identified, it is worth questioning the nature of α_3 and α_4. In particular, it is tempting to consider α_3 as a consequence of $|S_0^{*,e} \times s_h^{*,h}\rangle$ TPE [Fig. 3(d)]. However, in the SPA, this state would present a resonance at $J_{ee} + J_{hh} \sim 7.5$ meV above the resonance associated with the TPE of $|\widetilde{T_0^e \times T_0^h}\rangle$. In fact, experimentally α_3 is located at $\sim$10 meV at higher energy [Fig. 3(c)]. This difference can be due to many-body effects, as already mentioned, but also to the anisotropic contributions of the interparticle exchange [20] which impacts the relative position of the singlet states. Moreover, it is also possible that α_3 and α_4 are associated with $s_e^1 s_h^1 p_e^1 d_e^1$ states involving d_h valence orbitals, which may thermalize to $s_e^1 s_h^1 p_e^1 p_h^1$. p_e-d_h transitions have indeed been identified by high-resolution PLE in the same type of dots [13].

IV. CONCLUSION

We have demonstrated a resonant two-photon excitation process where two electron-hole pairs can be absorbed simultaneously on different orbital levels in a quantum dot. The optically active triplet states corresponding to this four-particle complex $(s_e^1 s_h^1 p_e^1 p_h^1)$ have been identified. Two-photon excitation has also been used to address the singlet states of the levels' fine structure. The latter can relax to the triplet states, which in turn becomes a probe to identify the singlets. This excitation spectroscopy, whose resolution is limited by the spectral width of the pulsed laser, allowed us to estimate the exchange integrals J_{hh} and J_{ee} whose values are, respectively, $\sim$ 1.3 and $\sim$6.2 eV. These results have been confirmed by correlating the energy of the singlet states with their signatures on the PLE spectrum of the biexciton.

We have also shown that the electron-hole exchange interaction can not be the unique origin of the electron-hole flip-flop mechanism necessary for the singlet-triplet relaxation. The $|S_0^*\rangle - |T_0\rangle$ mixing induced relaxation process is made possible by the anisotropic part of the h-h exchange, as well as that associated with the e-e exchange [20].

This TPE process can be extended to the case of charged quantum dots, opening the way to optical control of the electronic spin localized on higher-energy orbital levels [30].

ACKNOWLEDGMENTS

This work was funded by the French National Research Agency (ANR "SPINEX" Grant No. ANR-17-CE30-0022-01 and ANR "ISQUAD" Grant No. ANR-18-CE47-0006-01), by the Paris Île-de-France Région in the framework of DIM SIRTEQ and by the Cluster of Excellence MATISSE led by Sorbonne Universités. A.B. and B.E. are grateful to the Quantum Information Center Sorbonne (QICS) for specific fundings. This work was partly supported by the french RENATECH network.

APPENDIX A: SINGLET-TRIPLET COUPLINGS INDUCED BY ELECTRON-HOLE EXCHANGE INTERACTION

We present in this Appendix the relevant matrix elements of the coupling between singlet and triplet states of the $s_e^1 s_h^1 p_e^1 p_h^1$. We consider here that this coupling comes from the anisotropic part of e-h exchange interaction. Table II shows the matrix elements $M_{f\leftarrow i} = \langle f|\hat{H}_{eehh}|i\rangle$. In the main text, we mention that the anisotropic part of the exchange interaction of identical particles (e and h) is at the origin of a singlet-triplet coupling in particular by mixing S_0^* and T_0.

TABLE II. Singlet-triplet mixing induced electron-hole exchange interaction induced in the $s_e^1 s_h^1 p_e^1 p_h^1$ configuration. Only the couplings to the spin-triplet states having an optical activity are expressed. The states $|1\rangle$ and $|2\rangle$ are expressed in Table I. $\Sigma_{++--} = \Delta_1^{s_e s_h} + \Delta_1^{s_e p_h} - \Delta_1^{p_e s_h} - \Delta_1^{p_e p_h}$ and $\Sigma_{+--+} = \Delta_1^{s_e s_h} - \Delta_1^{s_e p_h} - \Delta_1^{p_e s_h} + \Delta_1^{p_e p_h}$. Note that the $\{\Delta_1^{ij}\}$ being all of the same magnitude, Σ_{++--} and Σ_{+--+} are small compared to the h-h and e-e exchange energies. Therefore, the anisotropic e-h exchange interaction plays a negligible role in the singlet-triplet relaxation.

$M_{f\leftarrow i}$	$\lvert S_0^{*,e} \times S_0^{*,h}\rangle$	$\lvert S_0^{*,e} \times T_0^h\rangle$	$\lvert T_0^e \times S_0^{*,h}\rangle$
$\langle 1\rvert$	$-\frac{1}{2\sqrt{2}}\Sigma_{+--+}$	0	0
$\langle 2\rvert$	0	$\frac{1}{2\sqrt{2}}\Sigma_{++--}$	$-\frac{1}{2\sqrt{2}}\Sigma_{++--}$
$\langle \widetilde{T_0^e \times T_0^h}\rvert$	$\frac{\tilde{\Delta}_1}{2\sqrt{2}\tilde{\Delta}_0}\Sigma_{+--+}$	0	0

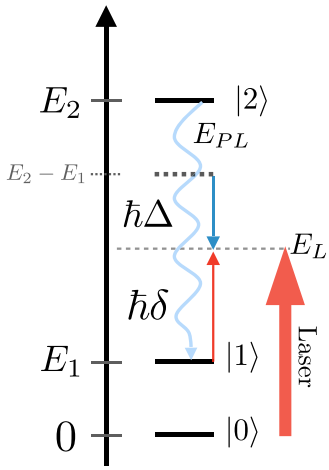

FIG. 4. Level diagrams describing the two-photon excitation process in the case where E_2 and $2E_1$ differ widely. $\hbar\Delta = E_L - (E_2 - E_1)$, $\hbar\delta = E_L - E_1$, and $E_{PL} = E_2 - E_1$. Two distinct Rabi couplings are used to account for two different oscillator strengths of the $0 \rightarrow 1$ and $1 \rightarrow 2$ optical transitions. See the main text for more details.

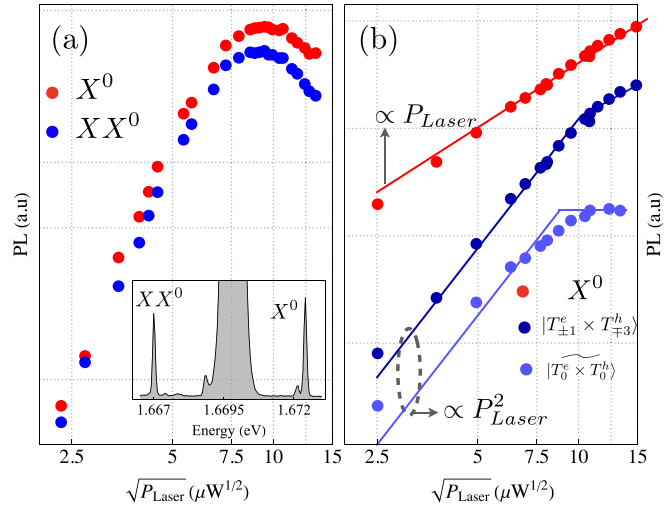

FIG. 5. (a) X^0 and XX^0 PL intensities as a function of $\sqrt{P_{\text{laser}}}$ for the conventional TPE process. Inset: luminescence spectra of X^0 and XX^0 while the laser is tuned to the TPE energy. (b) Same evolution for the p-shell recombination of $|T^e_{\pm1} \times T^h_{\mp3}\rangle$ and $|\widetilde{T^e_0 \times T^h_0}\rangle$, when the laser energy is set to their respective TPE resonance. The X^0 dependence is shown in the same experimental conditions.

APPENDIX B: TWO-PHOTON EXCITATION WITH DIFFERENT OPTICAL COUPLINGS

The TPE process described in this work involves two types of optical transitions related to s and p orbital levels. It is therefore desirable to describe the TPE process with two different Rabi frequencies [31] Ω_{01} and Ω_{12} (see Fig. 4). The two-photon excitation Hamiltonian reads as

$$\hat{H}(t) = \hat{H}_0 + \hat{H}_L(t), \tag{B1}$$

with $\hat{H}_0 = E_1|1\rangle\langle 1| + E_2|2\rangle\langle 2|$ and $\hat{H}_L(t) = \hbar\Omega_{01}(t)|0\rangle\langle 1| + \hbar\Omega_{12}(t)|1\rangle\langle 2| + \text{H.c.}$ The corresponding eigenvector $|\psi(t)\rangle$ is computed in the rotating-wave approximation (RWA), and in particular the probability associated with the TPE process $P_2(t) = |\langle 2|\psi(t)\rangle|^2$ is derived using the following reasonable assumptions: the width of the laser pulse τ_p is much smaller than (i) the detuning $\delta = (E_L - E_1)/\hbar$ between the laser and E_1, i.e., $\delta\tau_p \gg 1$, and (ii) the pulsation difference $\Delta = (E_L - E_2 + E_1)/\hbar$, i.e., $|\Delta|\tau_p \gg 1$, and finally (iii) $\sup|\Omega_{01}(t)|$, $\sup|\Omega_{12}(t)| \ll \delta, |\Delta|$. Under these conditions, the optical response of the system becomes quasi-independent of the shape of the optical pulse, and $P_2(t) \ll 1$. This is why we can assume a rectangular pulse envelope of temporal width τ_p, i.e., $\Omega_{if}(t) = \Omega^0_{if} h(\frac{t-\tau_p}{\tau_p}) e^{-i\omega_L t}$, where $h(t)$ is the box distribution, and $\omega_L = E_L/\hbar$ the laser pulsation. We find then that the probability of preparing the system in state $|2\rangle$ just after the passage of the optical pulse:

$$P_2(\tau_p) \sim \frac{\left(\Omega^0_{01}\Omega^0_{12}\right)^2}{\delta^2}\tau_p^2 \text{sinc}^2\left(\frac{\tau_p(\Delta+\delta)}{2}\right), \tag{B2}$$

where $\text{sinc}x = \sin x/x$. P_2 clearly shows a resonant response at the vicinity of $\Delta + \delta = 0$, i.e., $E_L = E_2/2$ or $E_L = (E_{PL} + E_1)/2$ (see Fig. 4).

Moreover, the probability of TPE depends on the product $(\Omega^0_{01}\Omega^0_{12})^2$ leading to a quadratic dependence with the laser power of the signal associated with TPE [Fig. 5(b)]. We recall here that the relation between the Rabi frequency and the oscillator strength f_{mn} is $f_{mn} \propto (\Omega^0_{mn})^2$. This relationship is used to discard the nonaddressable triplet states by TPE in Sec. III.

Also, we notice that the expression (B2), which is only valid in the high detuning regime, provides an estimate of the width at half-resonance height of $2.4 \times 2\hbar/\tau_p \sim 0.5$ meV for $\tau_p = 6$ ps in good agreement with the width of the TPE resonance shown in Figs. 2(a) and 2(b). Conventional TPE is usually achieved in the Rabi regime [32–34]. Figure 5(a) shows one Rabi oscillation of both X^0 and XX^0 as a function of $\sqrt{P_{\text{laser}}}$, when the laser is tuned to the TPE condition. On the contrary, Fig. 5(b) shows a different behavior for the evolution of the PL intensity versus $\sqrt{P_{\text{laser}}}$ for the $|T^e_{\pm1} \times T^h_{\mp3}\rangle$ and $|\widetilde{T^e_0 \times T^h_0}\rangle$ transitions when the laser is tuned at their respective TPE resonance. A saturation regime is observed with a quadratic dependence at low power (see Appendix B), while X^0 signal keeps a linear dependence [35]. This difference observed between the two TPE experiments is due, in the first case to the small laser detuning $\hbar\delta = 2.5$ meV from the exciton line while it is four times more important in the second one where $\hbar\delta \sim 10$ meV. For the case of the exciton-biexciton transition, $\tau_p\delta$ remains comparable to unity, thus keeping the Rabi regime. However, for the exciton-triplet TPE process, $\tau_p\delta \gg 1$ suppressing Rabi oscillation [36], as can also be seen from Eq. (B2) valid for large laser detuning.

APPENDIX C: HYBRID TRANSITIONS

The experimental results shown in Fig. 3 highlight the role of $s^1_e s^1_h p^1_e p^1_h$ singlet states and the possible relaxation mechanisms assisted by e-h flip-flop and acoustic phonon emission. Here, we will again trace the signature of these states, by mea-

suring the biexciton PL where two carriers of the same nature are paired on the *s* level, while the other two are delocalized on the two orbital levels. These excited states are probed through *a priori* parity forbidden transitions of the envelope functions, which are here called hybrid.

The TPE of the triplet states being a resonant mechanism, it depends on the oscillator strength associated to the optical transition between the exciton and the triplet state (Appendix B). Under the assumption $\widetilde{\Delta}_2, \widetilde{\Delta}_1 \gg \widetilde{\Delta}_0$ the ratio of the oscillator strength between $|T_0^e \times T_0^h\rangle$ and $|T_{\pm1}^e \times T_{\mp3}^h\rangle$ is calculated to be 1:4, while it is experimentally 1:6 [see Figs. 3(a) and 3(b)]. This difference can be partly explained by the different relaxation dynamics of the considered triplet state, in particular when p_e^1, p_h^1 relaxes to s_e^1, s_h^1, respectively. The existence of such a mechanism is confirmed by the presence of specific spectroscopic features in the PL at the expected energy of the s_e-p_h and p_e-s_h transitions [37].

Figure 6(a) shows the luminescence spectrum in the intermediate region when the *ps*-laser energy is near the TPE resonance. This spectrum reveals a doublet structure labeled ϵ_1, ϵ_2 at 10 meV below the *p*-shell recombination of $(s_e^1 s_h^1 p_e^1 p_h^1)_{\text{triplet}}$, as well as another doublet labeled β_1, β_2 located at 13 meV below, to which is linked a weak isolated peak labeled β_3.

The PL intensity of the main components β_2, ϵ_2 in Figs. 6(b) and 6(c) shows a quadratic dependence with laser power, indicating a biexciton behavior. The resonant behavior of the PL [Figs. 5(d) and 5(e)] as the laser scans the TPE area of the $(s_e^1 s_h^1 p_e^1 p_h^1)_{\text{triplet}}$, demonstrates the connection with triplets states through nonradiative channels. Moreover, the ϵ_2 peak has a second resonance when the laser energy is set to the $|T_0^e \times S_0^{*,h}\rangle$ TPE condition already identified as α_1 in Sec. III, and thus validating its interpretation. This points out a relaxation mechanism from $S_0^{*,h}$ to S_0^h. All these findings unambiguously indicate that the ϵ lines are associated with p_e-s_h recombination from $s_e^1 s_h^2 p_e^1$, while the s_e-p_h emission from $s_e^2 s_h^1 p_h^1$ forms the β lines.

The inset of Fig. 6 shows the fine structure of $s_e^2 s_h^1 p_h^1$. $s_e^1 s_h^2 p_e^1$ has an identical and symmetric FS. The recombination from $|S_0^e \times S_0^{*,h}\rangle$ to the bright exciton corresponds to the β_3 line, and allows to evaluate $J_{hh} \sim 1.7$ meV. From the results discussed in the previous section, J_{hh} was estimated to be 1.3 meV. This difference could again be explained by many-body effects induced renormalization of the energy difference between singlet and triplet states depending on the kind of excitonic complex.[2] Moreover, the emission of transitions forbidden by the symmetry of the envelope functions may come from Coulomb renormalization itself. Finally, these results are corroborated by noting that the splitting between β_2 and β_1 as well as between ϵ_2 and ϵ_1 are identical and consistent with the dark and bright exciton splitting evaluated to be 240 μeV for this dot.

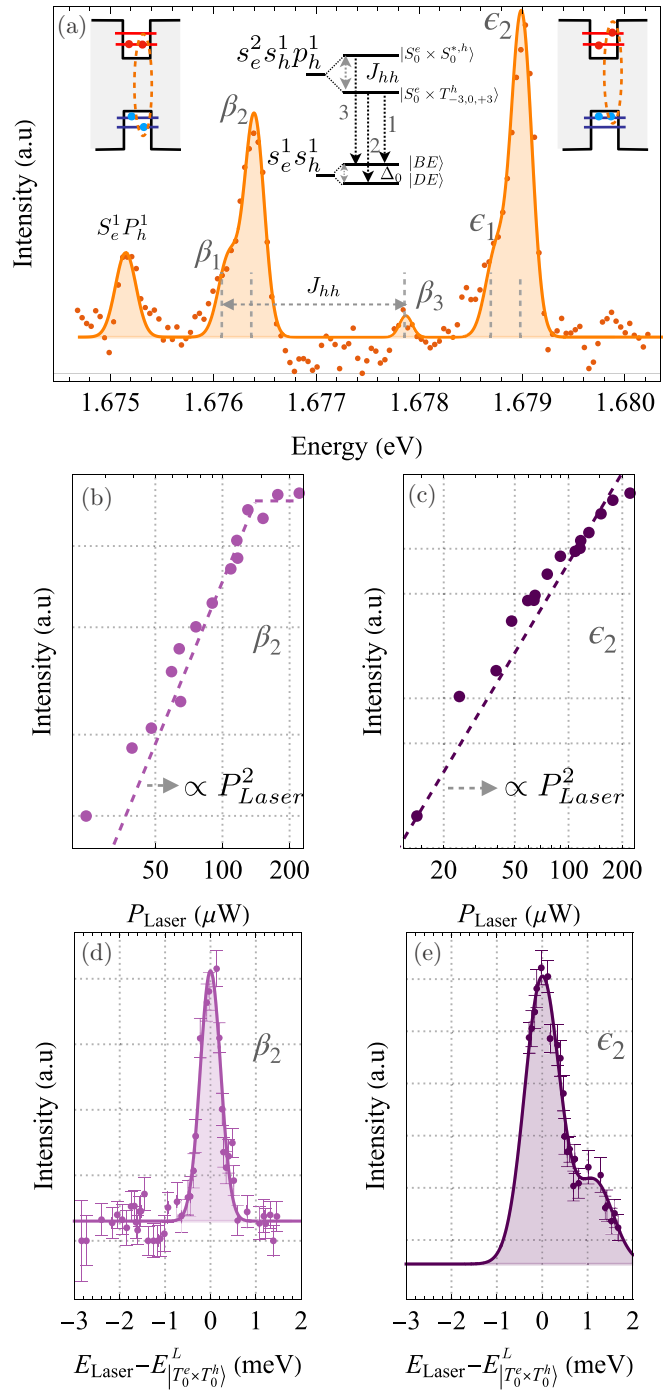

FIG. 6. (a) PL spectra of the p_e-s_h and s_e-p_h transitions from the biexcitonlike complexes $s_e^1 s_h^2 p_e^1$ and $s_e^1 s_h^2 p_h^1$, when the laser is tuned to the energy of the $(s_e^1 s_h^1 p_e^1 p_h^1)_{\text{triplet}}$ TPE condition. The inset represents the levels diagram and the emission paths for $s_e^2 s_h^1 p_h^1$. The *s*-shell recombination of $|T_{\pm1}^e \times T_{\mp3}\rangle$ allows to detect the signal from $s_e^1 p_h^1$ indicated by the line at 1.6752 eV. (b), (c) PL intensity of β_2 and ϵ_2 as a function of the laser power. (d), (e) PLE intensity of β_2 and ϵ_2 as a function of the *ps*-laser energy. The resonant line of ϵ_2 is incomplete on the low-energy side due to the increase of the laser scattering.

[2]Even for InAs dots, and more particularly for the case of positively charged complexes, a slight deviation from the expected SPA FS has been measured and theoretically calculated [20]. This deformation, although weak for InAs QDs, is all the more important for the case of positively charged complexes due to the small energy difference between the different valence levels, maximizing the many-body-effects induced mixing.

[1] P. Senellart, G. Solomon, and A. White, Nat. Nanotechnol. **12**, 1026 (2017).

[2] O. Benson, C. Santori, M. Pelton, and Y. Yamamoto, Phys. Rev. Lett. **84**, 2513 (2000).

[3] M. Müller, S. Bounouar, K. D. Jöns, M. Glässl, and P. Michler, Nat. Photonics **8**, 224 (2014).

[4] R. Winik, Phys. Rev. B **95**, 235435 (2017).

[5] I. Schwartz, Science **354**, 434 (2016).

[6] G. Peniakov, Phys. Rev. B **101**, 245406 (2020).

[7] P. Atkinson, E. Zallo, and O. G. Schmidt, J. Appl. Phys. **112**, 054303 (2012).

[8] S. Germanis, P. Atkinson, R. Hostein, S. Suffit, F. Margaillan, V. Voliotis, and B. Eble, Phys. Rev. B **102**, 035406 (2020).

[9] S. Germanis, P. Atkinson, R. Hostein, C. Gourdon, V. Voliotis, A. Lemaître, M. Bernard, F. Margaillan, S. Majrab, and B. Eble, Phys. Rev. B **98**, 155303 (2018).

[10] S. Germanis, P. Atkinson, R. Hostein, S. Majrab, F. Margaillan, M. Bernard, V. Voliotis, and B. Eble, Phys. Rev. B **104**, 115306 (2021).

[11] S.-Y. Shiau, B. Eble, V. Voliotis, and M. Combescot, Phys. Rev. B **101**, 161405(R) (2020).

[12] See Supplemental Material at http://link.aps.org/supplemental/10.1103/PhysRevB.105.235430 for a set of complementary experimental results confirming the interpretations given in the main paper. These experiments were performed with a continuous laser allowing to describe and complete the non-trivial radiative cascade inherent to the two electron-hole pair excitonic complex addressed by two-photon excitation. The Supplemental Material includes a reference to E. R. Schmidgall, I. Schwartz, D. Cogan, L. Gantz, T. Heindel, S. Reitzenstein, and D. Gershoni, Appl. Phys. Lett. **106**, 193101 (2015).

[13] C. Hopfmann, N. L. Sharma, W. Nie, R. Keil, F. Ding, and O. G. Schmidt, Phys. Rev. B **104**, 075301 (2021).

[14] O. Verzelen, R. Ferreira, and G. Bastard, Phys. Rev. B **62**, R4809 (2000).

[15] Y. Benny, Y. Kodriano, E. Poem, S. Khatsevitch, D. Gershoni, and P. M. Petroff, Phys. Rev. B **84**, 075473 (2011).

[16] B. Urbaszek, R. J. Warburton, K. Karrai, B. D. Gerardot, P. M. Petroff, and J. M. Garcia, Phys. Rev. Lett. **90**, 247403 (2003).

[17] D. Huber, B. U. Lehner, D. Csontosová, M. Reindl, S. Schuler, S. F. Covre da Silva, P. Klenovský, and A. Rastelli, Phys. Rev. B **100**, 235425 (2019).

[18] H. Huang, D. Csontosová, S. Manna, Y. Huo, R. Trotta, A. Rastelli, and P. Klenovský, Phys. Rev. B **104**, 165401 (2021).

[19] D. Csontosová and P. Klenovský, Phys. Rev. B **102**, 125412 (2020).

[20] T. Warming, E. Siebert, A. Schliwa, E. Stock, R. Zimmermann, and D. Bimberg, Phys. Rev. B **79**, 125316 (2009).

[21] H. Kamada, H. Ando, T. Takagahara, J. Temmyo, and T. Tamamura, J. Lumin. **87-89**, 46 (2000).

[22] H. V. A. Galeti, H. B. de Carvalho, M. J. S. P. Brasil, Y. Galvão Gobato, V. Lopez-Richard, G. E. Marques, M. Henini, and G. Hill, Phys. Rev. B **78**, 165309 (2008).

[23] F. Findeis, A. Zrenner, G. Böhm, and G. Abstreiter, Phys. Rev. B **61**, R10579 (2000).

[24] M. Vidal, Contrôle optique des spins électroniques et nucléaires dans un nano-objet unique : vers le développement de nano-mémoires et d'applications en imagerie, Ph.D. thesis, INSA Toulouse, 2016, https://tel.archives-ouvertes.fr/tel-01511091.

[25] M. E. Ware, E. A. Stinaff, D. Gammon, M. F. Doty, A. S. Bracker, D. Gershoni, V. L. Korenev, Ş. C. Bădescu, Y. Lyanda-Geller, and T. L. Reinecke, Phys. Rev. Lett. **95**, 177403 (2005).

[26] S. Laurent, M. Senes, O. Krebs, V. K. Kalevich, B. Urbaszek, X. Marie, T. Amand, and P. Voisin, Phys. Rev. B **73**, 235302 (2006).

[27] K. V. Kavokin, Phys. Rev. B **69**, 075302 (2004).

[28] Ş. C. Bădescu, Y. B. Lyanda-Geller, and T. L. Reinecke, Phys. Rev. B **72**, 161304(R) (2005).

[29] S. G. Carter, Phys. Rev. Lett. **126**, 107401(R) (2021).

[30] C. Spinnler, L. Zhai, G. N. Nguyen, J. Ritzmann, A. D. Wieck, A. Ludwig, A. Javadi, D. E. Reiter, P. Machnikowski, R. J. Warburton, and M. C. Löbl, Nat. Commun. **12**, 6575 (2021).

[31] C. Aslengul, in *Mécanique Quantique: Développements et Applications à Basse Énergie*, edited by D. Boeck, Vol. 2 (de Boeck Supérieur, 2018).

[32] D. Huber, M. Reindl, Y. Huo, H. Huang, J. S. Wildmann, O. G. Schmidt, A. Rastelli, and R. Trotta, Nat. Commun. **8**, 15506 (2017).

[33] E. Schöll, L. Schweickert, L. Hanschke, K. D. Zeuner, F. Sbresny, T. Lettner, R. Trivedi, M. Reindl, S. F. Covre da Silva, R. Trotta, J. J. Finley, J. Vučković, K. Müller, A. Rastelli, V. Zwiller, and K. D. Jöns, Phys. Rev. Lett. **125**, 233605 (2020).

[34] S. Bounouar, M. Müller, A. M. Barth, M. Glässl, V. M. Axt, and P. Michler, Phys. Rev. B **91**, 161302(R) (2015).

[35] G. Juska, I. Ranjbar Jahromi, F. Mattana, S. Varo, V. Dimastrodonato, and E. Pelucchi, Appl. Phys. Lett. **117**, 134001 (2020).

[36] S. Stufler, P. Machnikowski, P. Ester, M. Bichler, V. M. Axt, T. Kuhn, and A. Zrenner, Phys. Rev. B **73**, 125304 (2006).

[37] Y. Kodriano, E. Poem, N. H. Lindner, C. Tradonsky, B. D. Gerardot, P. M. Petroff, J. E. Avron, and D. Gershoni, Phys. Rev. B **82**, 155329 (2010).